Catalysis Science & Technology

ROYAL SOCIETY OF CHEMISTRY

PAPER

View Article Online
View Journal | View Issue

Cite this: *Catal. Sci. Technol.*, 2025, **15**, 2016

Nonthermal plasma integrated with catalysts for nitrogen fixation from nitrogen and water†

Yanna Liu, Zhaofei Li and Hua Song *

Received 30th November 2024,
Accepted 29th January 2025

DOI: 10.1039/d4cy01446d

rsc.li/catalysis

Directly synthesizing NH_3 and NO_x from N_2 and H_2O by nonthermal plasma (NTP) at atmospheric pressure and low temperature is considered an attractive alternative for the Haber–Bosch process. Nonthermal plasma integrated with a catalyst was employed to investigate the effect of metal-impregnated SBA-15 on nitrogen fixation efficiency. The results demonstrated that the total nitrogenous product synthesis rate reached 140.78 μmol h^{-1} with an energy yield of 597.32 mg_N kW^{-1} h^{-1} when the Ni-SBA-15 catalyst was employed. In the reaction, HNO_2 reacts with NH_3 to form NH_4NO_2, rapidly decomposing into N_2 and H_2O, responsible for production distribution. The addition of Ni-SBA-15 promotes plasma-activated species, resulting in nitrogen fixation efficiency. This work lays the foundation for studying nitrogen fixation driven by the NTP-catalyst integrated system.

Introduction

Nitrogen is essential for biological growth and metabolism, so nitrogen fixation is vital in ecosystems and agriculture.[1] However, nitrogen in the atmosphere is usually challenging for organisms to utilize directly due to its triple-bond solid chemical structure, so it needs to be converted by nitrogen fixation. Nitrogen fixation is a process of converting atmospheric nitrogen (N_2) into biologically available nitrogen compounds such as ammonia (NH_3) or nitrate/nitrite (NO_3^-/NO_2^-).[2] Nitrogen fixation is not only helpful for plant growth and ecological balance but also benefits the reduction of dependence on synthetic fertilizers.

Nitrogen fixation can be categorized into biological,[3–5] natural, and industrial processes. Biological nitrogen fixation usually occurs in soil or water and is realized by certain bacteria converting atmospheric nitrogen into NH_3, which will be further converted to NO_3^-. Based on the conversion process, some limitations remain, such as only occurring on certain bacteria, being susceptible to pH, temperature, and humidity, and being hard to control.[5] Natural nitrogen fixation refers to lightning-assisted converting N_2 to NO_x, which is dissolved by rain to form NO_3^- and NO_2^-. The Haber–Bosch process has been the cornerstone of industrial nitrogen fixation for over a century. However, it operates under harsh conditions (high temperature of 450–600 °C and pressure of 150–350 atm)[6] and relies on hydrogen derived from fossil fuels, leading to significant carbon emissions and energy consumption.[7,8] Hence, many green, environmentally friendly, and mild methods were developed, including the electrochemical nitrogen reduction reaction,[9–11] photocatalytic reaction[12,13] and plasma-assisted process.[14,15] Among them, plasma-assisted nitrogen fixation allows obtaining NH_3 or NO_x at lower temperatures and pressure, particularly integrating with catalysts, remarkably improving energy efficiency and yield. Many highly reactive species, such as electrons, ions, excited molecular species, radicals, atoms, and photons, are generated by the plasma discharge process, which facilitates nitrogen fixation. Furthermore, plasma-assisted nitrogen fixation allows for decentralized and modular setups that can be easily scaled up or down, providing flexibility in production capacity.[1,16,17]

Nitrogen fixation by plasma is an exciting and promising technology, but its implementation is far from simple. The complexity of nitrogen fixation by plasma arises from a combination of factors, including the physics of plasma formation, the intricate chemical reactions involved, and the design of effective reactor systems.[18] Plasma discharge directly affects how nitrogen molecules are activated and converted into reactive nitrogen compounds, which has aroused interest in recent years.[18,19] A variety of plasma has been investigated for nitrogen fixation, including dielectric barrier discharge (DBD),[20,21]gliding arc,[22,23] magnetically stabilized glow discharge,[24] and microwave plasma.[25,26] Zhou *et al.*[27] analyzed the energy efficiency (EE) and yield of various discharge types and concluded that the most efficient configuration is a dielectric barrier discharge (DBD) driven by pulsed voltage. Patil *et al.* explored the NTP NO_x synthesis in a packed bed DBD reactor with different catalysts. It was

Department of Chemical and Petroleum Engineering, University of Calgary, Calgary T2N 1N4, Canada. E-mail: sonh@ucalgary.ca

† Electronic supplementary information (ESI) available. See DOI: https://doi.org/10.1039/d4cy01446d

found that the support materials and their particle sizes had an essential effect on the concentration of NO_x.[20] Li *et al.*[28] investigated the influences of the applied voltage, discharge power, and flow rate on the reaction performance. The results indicated that higher flow rates led to lower ammonia concentration and lower energy consumption. Notably, plasma-assisted nitrogen fixation is a reaction process regulated by multiple parameters.

In plasma-based nitrogen fixation, water (either as an electrode or part of the gas stream) has gained significant attention as a green hydrogen source capable of generating reactive oxygen and nitrogen species. Applying a corona discharge over a water surface increased NO_x conversion to HNO_2/HNO_3 by over 90% compared to cases without water, significantly reducing the need for downstream aqueous scrubbers to capture plasma-produced gaseous NO_x.[29,30] Kubota *et al.*[31] obtained ammonium and nitric acid by injecting a nitrogen plasma jet into pure water. With the aid of UV irradiation, the ammonium synthesis rate is enhanced when nitrogen plasma gas is purified into water.[32] A nonthermal plasma (NTP)-assisted nitrogen fixation process was employed to ensure adequate contact of gas and liquid by configuring water-falling film along with the reactor.[33]

Catalysts are crucial in plasma-assisted nitrogen fixation as they enhance reaction efficiency, improve nitrogen adsorption, and facilitate the conversion of nitrogen to ammonia and other nitrogen compounds. However, only a few researchers have investigated the plasma–catalyst integrated system for the reaction of N_2 and H_2O. Pd–Al_2O_3 was integrated with plasma to generate H_2 and NO_x from H_2O and N_2, resulting in catalytic reduction of NO_x by H_2.[34] Ru/MgO catalysts were introduced into NTP-assisted reaction with N_2 and H_2O, and it was found that the synergistic effect of plasma and catalyst promoted the ammonia production rate.[35] Therefore, developing new nitrogen fixation catalysts and exploring the mechanisms of plasma-catalytic reactions is essential for creating energy-efficient, sustainable methods that use water as a hydrogen source rather than fossil fuels. It potentially reduces greenhouse gas emissions while improving nitrogenous compound production rates and selectivity, making it a promising pathway for green fertilizer synthesis.

In this work, nitrogen fixation from liquid water and N_2 is performed with the assistance of NTP catalysis. Different metal-impregnated SBA-15 (Ni, Fe, Cu) served as catalysts and were evaluated in terms of catalytic performances. The synergistic effect between the catalyst and plasma is verified by comparing the experiment without and with catalysts. The physical and chemical properties were also characterized to investigate the influence of catalysts on the reaction.

Experimental section

Catalyst preparation

5% (wt%) metal (Ni, Fe, and Cu)-loaded SBA-15 catalysts were obtained by hydrothermally synthesizing SBA-15 followed by wet impregnation of metal on the support of SBA-15. The details of the synthesis of SBA-15 are presented in a previous study.[36] In the synthesis process, poly-(ethylene glycol)–poly-(propylene glycol)–poly-(ethylene glycol) block copolymer (Pluronic P123, Aldrich) is applied as a template reagent. The molar ratio of the reactants added into the system is as follows – TEOS : HCl : H_2O : P123 = 60 : 78 : 6000 : 1. At first, P123 was dissolved in a hydrochloric acid aqueous solution by stirring. Then, tetraethyl orthosilicate (TEOS, 98%, Aldrich) was added into the above mixture drop by drop and left stirring for 24 h, followed by pouring into a sealed reagent bottle to crystallize at 100 °C for another 24 h. The solid product was collected by filtering and washing with deionized (DI) water several times until the pH value of the filtrate reached 6–7. After that, the sample SBA-15 was obtained by placing it in the oven at 80 °C overnight and calcined in a muffle furnace at 550 °C for 5 h.

The metal-loaded catalysts were synthesized using the incipient wetness impregnation method. The metallic nitrates ($Ni(NO_3)_2$, $Fe(NO_3)_3$, and $Cu(NO_3)_2$) were employed as precursors and prepared as the corresponding aqueous solutions. The SBA-15 powder was added to the above aqueous solution by vigorously stirring and mixing. The resulting mixture remained still for 3 h at room temperature and then dried overnight at 80 °C. Lastly, the obtained solids were calcined at 500 °C for 4 h with a ramp rate of 5 °C min^{-1}. All the samples were reduced by calcining in 5% H_2/Ar flow at 550 °C for 1 h with a heating ramp of 5 °C min^{-1}. The acquired samples were denoted as Ni-SBA-15, Fe-SBA-15, and Cu-SBA-15, respectively.

Performance evaluation

Experimental setup. The experimental apparatus is shown in Fig. 1. The reactor is made of quartz, with an outer diameter of 10 mm and thickness of 1 mm. A stainless-steel rod is placed at the center of the quartz tube, connected to the plasma generator, acting as a high-voltage electrode. Meanwhile, an iron mesh wraps the quartz tube and serves

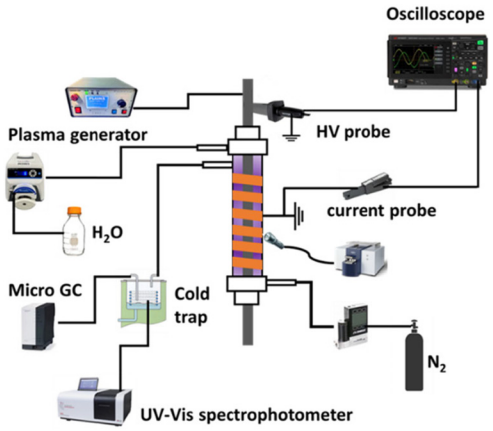

Fig. 1 Schematic diagram of N fixation from N_2 and H_2O with the assistance of plasma.

as a grounding electrode. In the reaction, N_2 (ultra high purity, 99.99%, Air Liquide, Canada) is blown into the reactor from the bottom, controlled by a mass flow rate controller. The water is pumped into the reactor by a water pump. A LEAP100© plasma generator provided the microsecond pulsed plasma discharge with a pulse voltage of 0–80 kV pk–pk, a repetitive pulse frequency from 100 to 3000 Hz, and power up to 700 W. The electrical properties of the system are monitored by an oscilloscope (Keysight, DSOX 1204G Series), where a high-voltage probe (P6150A, Tektronix) and current probe (TCP202, Tektronix) are employed to measure the voltage and current, respectively.

In the typical catalytic performance evaluation experiment, 100 mg of powder catalyst was placed in the center of the reactor. Quartz wool was packed at the bottom and top of the catalyst bed, which hindered the catalyst's displacement. The reactor's temperature was controlled by cooling air at 50 °C, monitored by a thermal camera (FLIR One®). The outlet gas was absorbed by 0.005 mol L^{-1} H_2SO_4 in a reagent bottle immersed in a cold trap, followed by analysis with a UV-vis spectrophotometer to detect the concentration of NH_4^+, NO_3^- and NO_2^-. The specific method and reagents used in the detection are presented in the ESI.† The concentration of N_2 in the outlet is analyzed by micro gas chromatography (micro-GC, Agilent 490) after vapor condensation. Optical emission spectroscopy (OES) is employed to monitor the light emitted from the reactor *in situ*. A single-channel UV-vis-NIR spectrophotometer (Avantes Inc., USB2000 Series) accessorized with a fiber optic cable (400 μm) was applied to measure the emission spectra of the glow region located at the center of the reactor. The measured wavelength number was 200–800 nm, and the line grafting was 600 lines mm^{-1} with a resolution of 0.4 nm.

Calculation. Some parameters, such as discharge power (P), formation rate (r), yield, and energy yield, are essential for evaluating the catalytic performance of NTP-assisted N fixation. The parameters are calculated as follows.

$$P = f\int v(t)I(t)\mathrm{d}t \quad (1)$$

Here, $v(t)$ and $I(t)$ are the voltage and current measured by the oscilloscope, respectively. f is the pulse repetition frequency.

$$r_{NH_3} = \frac{C_{NH_4^+} \times V \times 60}{14 \times t} \quad (2)$$

$$r_{NO_3^-} = \frac{C_{NO_3^-} \times V \times 60}{14 \times t} \quad (3)$$

$$r_{NO_2^-} = \frac{C_{NO_2^-} \times V \times 60}{14 \times t} \quad (4)$$

$$r_{\text{total N}} = r_{NH_3} + r_{NO_3^-} + r_{NO_2^-} \quad (5)$$

$$\text{Yield} = \frac{r_{\text{total N}}}{\text{the amount of N input}} \quad (6)$$

$$\text{Energy yield} = \frac{r_{\text{total N}}}{\text{power}} \quad (7)$$

$C_{NH_4^+}$ (mg L^{-1}) is the concentration of NH_4^+ obtained from the absorption cell, which is measured by the UV-vis spectrum, V (mL) is the volume of the adsorption solution used in the experiment, t (minute) is the reaction time, m_c is the mass of catalysis, and 14 is the molar mass of N, respectively.

Catalyst characterization. The synthesized catalyst crystalline phase was measured by powder X-ray diffraction (XRD) analysis on a Bruker D8 Advance X-ray diffractometer with CuKα_1 radiation (λ = 1.5406 Å). The morphologies and crystalline structures of the samples were observed by scanning electron microscopy (SEM) and high resolution transmission electron microscopy (HRTEM), conducted on an FEI Quanta FEG 250 and Tecnai F20, respectively. The surface area and pore structure properties of the catalysts were obtained using a Micromeritics ASAP 2020 apparatus. The surface area was calculated by the Brunner–Emmett–Teller method (BET), and the total pore volume, average pore diameters, and pore size distributions were obtained from the N_2 adsorption branches of isotherms using the Barrett–Joyner–Halenda (BJH) method. Ammonia temperature-programmed desorption (NH_3-TPD) experiments were performed to study the acidity of the prepared catalyst by using a Micromeritics AutoChem II 2920 chemisorption analyzer.

Results and discussion

Catalysts' physicochemical properties

The XRD patterns of the prepared SBA-15, Ni-SBA-15, Fe-SBA-15, and Cu-SBA-15 are displayed in Fig. 2. The broad diffraction peak at 2θ = 23° in all the samples corresponds to the (111) plane of silica, attributed to the disordered Si–O–Si network in the mesoporous silica walls.[37] The diffraction peaks at 43.3° and 50.4° in the sample of Cu-SBA-15 were indexed as the (111) and (200) reflections of crystalline

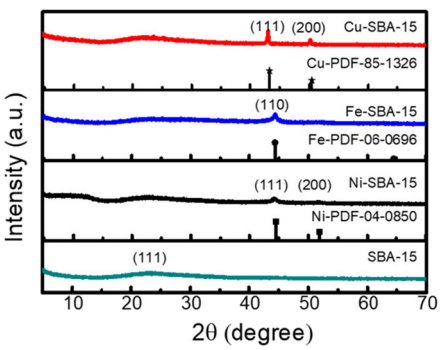

Fig. 2 XRD patterns of SBA-15, Ni-SBA-15, Fe-SBA-15 and Cu-SBA-15.

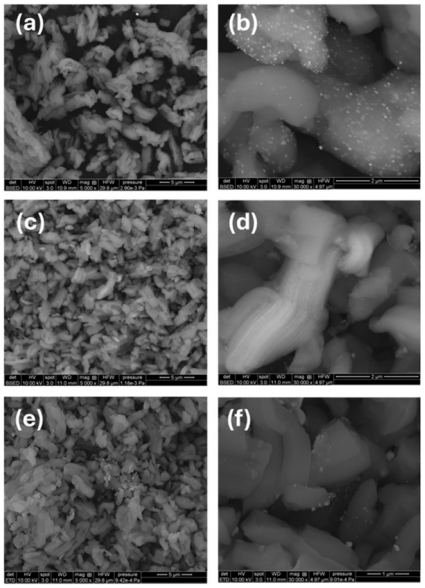

Fig. 3 SEM images of Ni-SBA-15 (a and b), Fe-SBA-15 (c and d), and Cu-SBA-15 (e and f).

metallic Cu (JCPDs file no. 85-1326).[38] The XRD pattern of Ni-SBA-15 shows two diffraction peaks at 2θ = 44.5° and 51.8°, which can be assigned to the (111) and (200) planes of Ni (JCPDs file no. 04-0850).[39] The diffraction peak at 44.67° belongs to the (110) crystal plane of Fe (JCPDs file no. 06-0696), indicating the existence of metallic Fe.[40] All the results indicate the successful impregnation of metals on the support of SBA-15.

The morphologies and structures of the prepared catalysts were characterized using SEM and TEM. The FESEM results are exhibited in Fig. 3. From Fig. 3(a), (c) and (e), it can be found that all the samples present the aggregations of worm-like rods with the length of the rod about 5–7 μm. The distributions of the particles are uniform. Fig. 3(b) shows that some nanoparticles are dispersed uniformly on the surface of the worm-like rods. However, no iron or iron oxide particles were observed on the surface of SBA-15, as shown in Fig. 3(d), indicating that most of the iron entered into the mesopore size of SBA-15.[40] From Fig. 3(f), it can be seen that some clusters appear on the surface of the support, which can be due to the higher surface energy of copper leading to agglomeration to reduce the total surface energy.[41]

Fig. 4 displays the HRTEM images of the prepared catalysts. It can be found that all the samples demonstrate the existence of cylindrical mesopores with well-ordered hexagonal arrays. The average diameter of the pore channels is about 7–8 nm, and the average pore wall thickness is about 3.5 nm. In the images of Fig. 4(a) and (b), the Ni nanoparticles are dispersed on the support of SBA-15 uniformly, and they are supported on both the exterior surface and the interior surface of the SBA-15 support, which are verified by the evidence of N_2 adsorption and desorption. In addition, we can find that the particles are somewhat aggregated into large particles. The high-resolution TEM

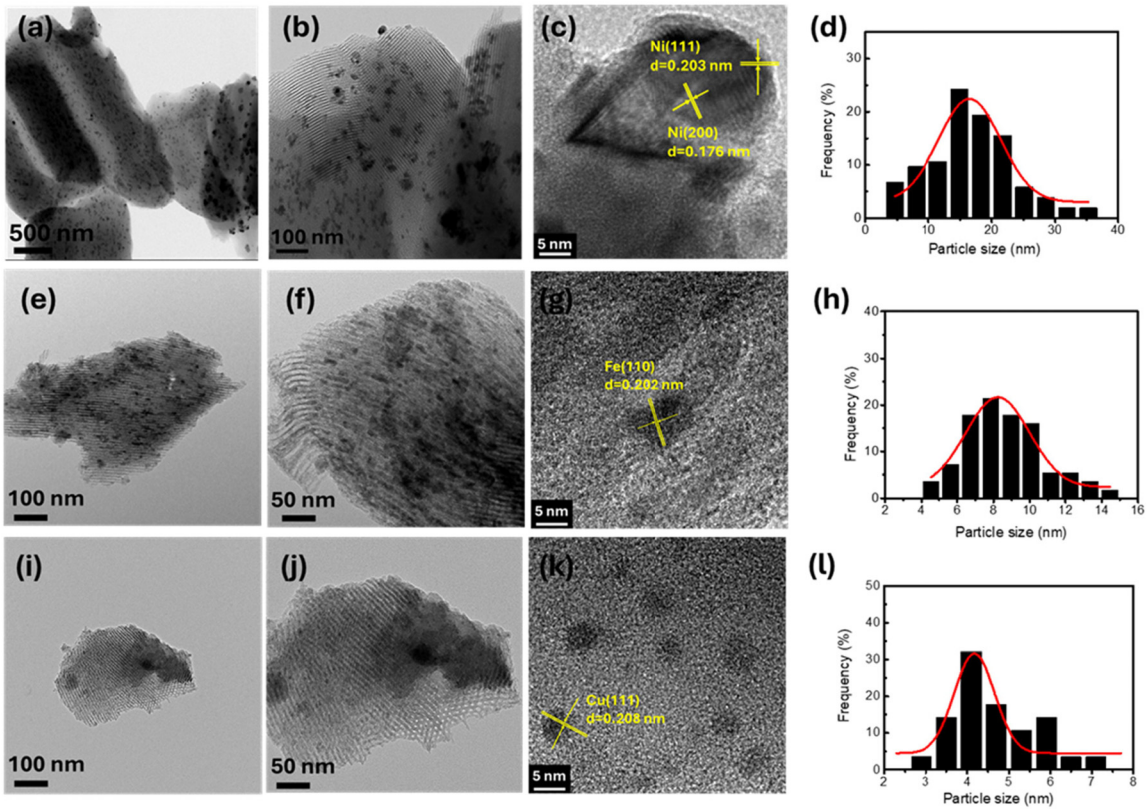

Fig. 4 HRTEM images of Ni-SBA-15 (a–c), Fe-SBA-15 (e–g), and Cu-SBA-15 (i–k) and particle size of Ni-SBA-15 (d), Fe-SBA-15 (h), and Cu-SBA-15 (l).

image in Fig. 4(c) shows the lattice fringes with vertical distances of 0.203 and 0.176 nm, corresponding to the interplanar spacing of the (111) and (200) planes of Ni particles.[42] From the particle size distribution in Fig. 4(d), most particles distribute with a size of 15 nm. From the images in Fig. 4(e) and (f), the Fe nanoparticles are significantly smaller than Ni nanoparticles and are mainly located in the interior of the SBA-15 pore channels. Fig. 4(h) displays the particle distribution and shows that the particles are about 8 nm. The nanoparticles with a crystal spacing of about 0.202 nm can be indexed to the crystal plane of (110) in Fe nanoparticles.[43] Small clusters are shown in Fig. 4(l), and Cu nanoparticles with a size of about 4 nm were found on the exterior and interior surfaces of the SBA-15 support, as shown in Fig. 4(i) and (j). The black spots in Fig. 4(k) are identified as Cu nanoparticles, which can be verified by the lattice spacing of 0.208 nm of the Cu plane (111).[44]

The surface area and pore structure of the catalysts play an essential role in the catalytic performance. Fig. 5 shows the N_2 adsorption–desorption isotherms and pore size distribution of the prepared catalysts. According to the IUPAC classification, all the isotherms of the catalysts exhibit the typical type IV behavior with a characteristic H1 hysteresis loop, indicating the uniform mesopores with one-dimensional cylindrical channels of SBA-15.[45,46] The impregnation of metal into the support of SBA-15 does not change the porous structure. However, the surface areas decrease (Table 1), and the order is as listed: SBA-15 > Cu-SBA-15 > Ni-SBA-15> Fe-SBA-15, which can be due to partial blockage of SBA-15 support pores with the corresponding metal particles. From Fig. 5(b), a unimodal distribution of pores in the 7–9 nm range is observed in SBA-15. With the impregnation of metals, the pore sizes become narrower than those of SBA-15, presenting around 5 nm, which agrees well with the average pore size displayed in Table 1. The order of pore size is the same as that of surface area. The decreased pore size can be attributed to some of the metal nanoparticles entering the pore channels of SBA-15 in the impregnation process.[47]

Table 1 Surface areas, pore volumes, and pore sizes of the catalysts

	BET surface area, $m^2\ g^{-1}$	Pore volume, $cm^3\ g^{-1}$	Pore size, nm
SBA-15	727	0.85	5.3
Ni-SBA-15	564	0.86	5.1
Fe-SBA-15	544	0.81	4.9
Cu-SBA-15	588	0.89	5.2

The surface acidity of the prepared catalysts was characterized by NH_3-TPD, and the results are presented in Fig. 6. It was found that no desorption peak appeared in the support SBA-15, indicating no acid site binding with NH_3. After loading Ni on SBA-15, there is a board peak from 150–400 °C on Ni-SBA-15, which can be assigned to weak acid sites (Lewis acid sites) resulting from the combination of Ni^{2+} and oxygen on the surface of SBA-15.[48,49] Compared with Ni-SBA-15, the intensity of the weak acid sites is much lower, indicating fewer acid sites in Fe-SBA-15. However, it can be seen that there are two small peaks between 300 and 500 °C, which can be attributed to the acidic sites formed by the interaction between Cu^{2+} and SBA-15.[50] The intensities of the two peaks are relatively low, implying only a tiny amount of acid sites formed in Cu-SBA-15.

Plasma diagnostics

Based on DBD reactor compositions, a dielectric barrier of the quartz tube and an air gap, where the gas is in contact with the plasma, are located between the high voltage and ground. Therefore, the corresponding DBD plasma discharge in the reactor can be indicated as the equivalent circuit in

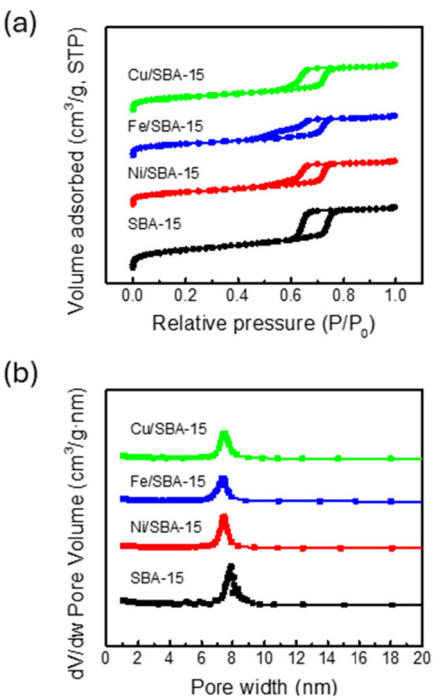

Fig. 5 N_2 adsorption–desorption isotherms (a) and pore size distributions (b) of SBA-15, Ni-SBA-15, Fe-SBA-15, and Cu-SBA-15.

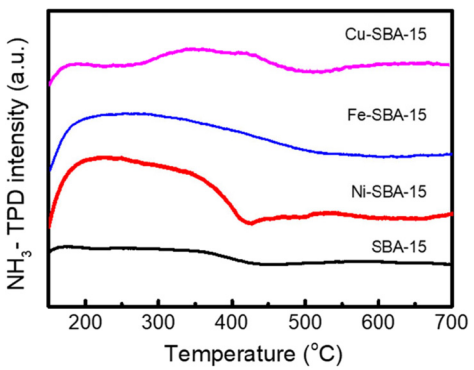

Fig. 6 NH_3-TPD spectra of SBA-15, Ni-SBA-15, Fe-SBA-15, and Cu-SBA-15.

Fig. 7(a).[51,52] Here, C_g is the capacitance of the gap, and C_d is the capacitance related to the dielectric barrier. Once the plasma discharge is carried on the reactor, the apparent capacitance of the DBD reactor is equivalent to the dielectric barrier capacitance of C_d. While the plasma discharge is off, the capacitance is regarded as a series connection of dielectric barrier capacitance and gap capacitance. R_{dis} is the plasma resistance in a parallel connection with C_g.

The discharge characteristics of the DBD reactor were recorded by the oscilloscope and are exhibited in Fig. 7(b). It can be observed that there are multiple pulses of voltage and current, the maximum amplitudes of which can reach 7.4 kV and 46.8 mA, respectively. The period of the active current pulse is about 500 μs. The instantaneous power is obtained from the multifaction of the instantaneous voltage and current, presented in Fig. 7(c). Here, the negative sign of the power indicates the opposite direction of the current or voltage. The active power is calculated from eqn (1). In our experiments, the discharge characteristics were measured three times, and the ultimate power was obtained from the average value of the active power. When the catalyst is packed in the DBD reactor, the average power was calculated as 3.30 ± 0.1 W.

Optical emission spectroscopy is employed to identify the possible species present in the NTP plasma-assisted catalytic reaction. The overall spectrum of the reactions with different catalysts is shown in Fig. 8(a). The results demonstrate that many forms of plasma-activated nitrogen species are present in the reactions, including vibrational and rotational excitation, electronic excitation, and ionization without dissociation.[35] The 220–300 nm peaks are assigned to the NO band, which is zoomed in Fig. 8(b). The spectrum shows NO ($A^2\Sigma^+$–$X^2\Pi$) molecular transitions in the plasma–catalytic process. NO-related peaks exhibited that NO was formed from the reactions between the N species and O or OH species in the plasma discharge process.[53–56] Comparing the corresponding peaks, all the normalized intensities for the NO band are higher for Ni-SBA-15 than the other catalysts, implying that the Ni-SBA-15 catalyst can improve the formation of NO-related excited radicals and species. The OH radical-induced peaks are observed in all the catalysts, and the intensity of Ni-SBA-15 is the highest, demonstrating that H_2O splitting generates OH species.[57]

Catalytic performance

Optimizing reaction conditions is essential to improving NTP reaction efficiency, selectivity, and stability. Therefore, control experiments were carried out on empty tubes, and

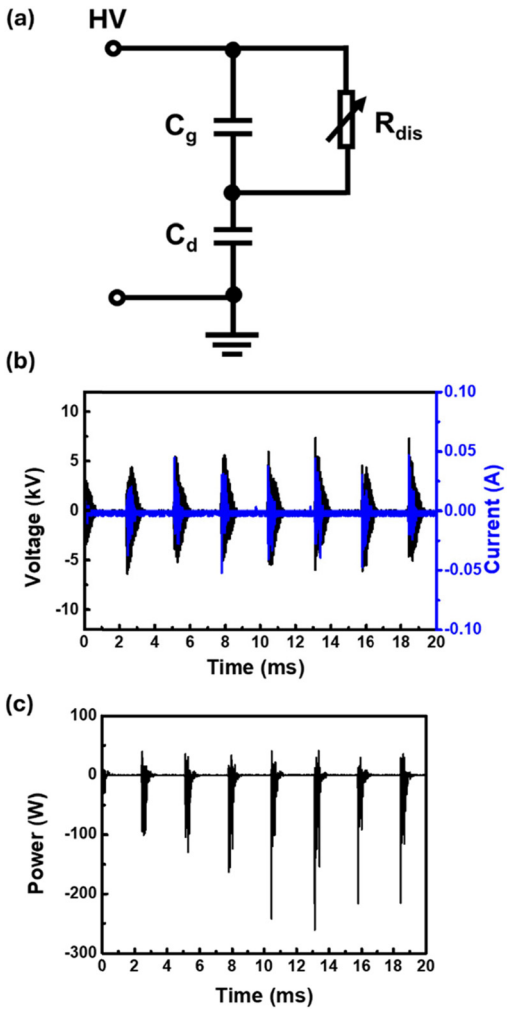

Fig. 7 (a) The equivalent circuit of the DBD reactor. (b) The typical voltage and current waveforms. (c) The instantaneous electric power for the DBD reactor.

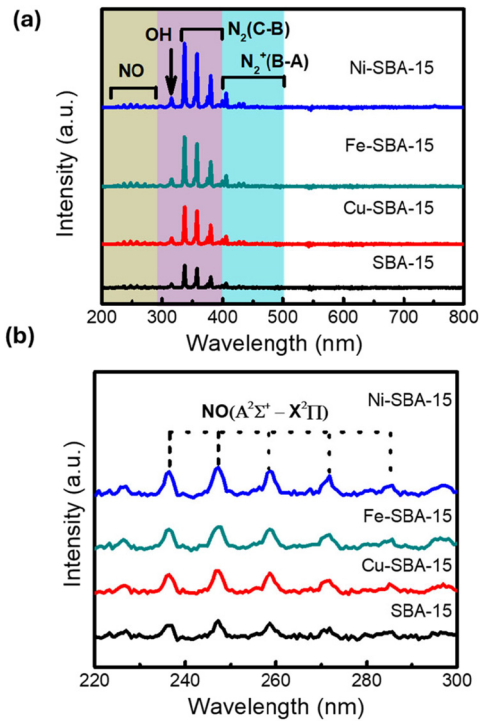

Fig. 8 The optical emission spectra of NTP plasma assisted N_2–H_2O reaction. (a) Overall OES spectrum (200–800 nm); (b) zoom-in OES spectrum of NO (220–300 nm).

the evaluation parameters were also compared to investigate the influence of the control impact factor on the reaction performances. We investigated the effect of N_2 (20, 40, 60, 80, and 100 mL min^{-1}) and H_2O (0.05, 0.10, and 0.15 mL min^{-1}) flow rate on the catalytic performance. From the control experiment results, the nitrogen fixation product is not only NH_3, but also NO_3^- and NO_2^-. The production rates of NH_3, NO_3^-, NO_2^- and total N with different N_2 and H_2O flow rates are displayed in Fig. 9(a). It can be found that the production rate of NO_3^- is significantly higher than NH_3, indicating that NO_x is predominately generated in the reaction. Therefore, it can be deduced that nitrogen fixation from N_2 and H_2O experienced two steps, including reactive species generating from the reactant molecule activation in the plasma discharge process and the reaction to form NH_3, NO_3^- and NO_2^-.[58] When the flow rate of H_2O is relatively low at 0.05 mL min^{-1}, all the production rates of NH_3, NO_3^-, NO_2^- and total N reach the highest with a N_2 flow rate of 20 mL min^{-1}. With the increment of N_2 flow rate from 20 to 40 mL min^{-1}, all the production rates decreased sharply and then stayed slightly changed through the increase of N_2 flow rate from 40 to 100 mL min^{-1}, which can be attributed to deficient contact between N_2 and H_2O related species. While the flow rate of H_2O is 0.10 mL min^{-1}, the production rates of NH_4^+, NO_3^- and total N exhibited a dramatic increase when the N_2 flow rate went from 20 to 40 mL min^{-1}, followed by a sharp decrease with 60 mL min^{-1} N_2 flow rate. Then, they gradually reduced to a low value. However, the production rate of NO_2^- remains stable, indicating that a limited amount of OH reacts with N species to form HNO_2. When the flow rate of H_2O increased to 0.15 mL min^{-1}, the trend of NO_3^-, NO_2^- and total N production is similar to that of 0.1 mL min^{-1} (H_2O flow rate). However, the NH_3 production rates are low and drop with the increment of the N_2 flow rate, which can be assigned to incomplete water splitting. Once the N_2 flow rate arrives at 40 mL min^{-1}, the production rate of both NH_3 and NO_3^- reaches the highest with 9.40 and 63.32 μmol h^{-1}, and the corresponding total N is 73.82 μmol h^{-1}. Therefore, in the following experiment, to evaluate the catalysts' performance, the reaction conditions are set as an H_2O flow rate of 0.1 mL min^{-1} and an N_2 flow rate of 40 mL min^{-1}.

Catalysts play a crucial role in plasma reactions, helping to improve the efficiency of the reaction and reducing energy consumption. The catalyst's surface can adsorb and activate the reactants, provide the necessary reactive sites, and promote the reaction. In addition, a synergistic effect might occur during the reaction, which benefits the target reaction.[34] In this work, the impact of metal active centers on the efficiency of nitrogen fixation from N_2 and H_2O is investigated by impregnating Ni, Fe, and Cu on SBA-15. The production rates of NH_3, NO_3^-, and NO_2^- produced from N_2 and H_2O with and without catalysts are displayed in Fig. 10(a). With the addition of SBA-15, it is evident that all the production rates are boosted because of the large surface area, allowing more reactive species to be adsorbed for reaction, such as nitrogen species, hydrogen species, and

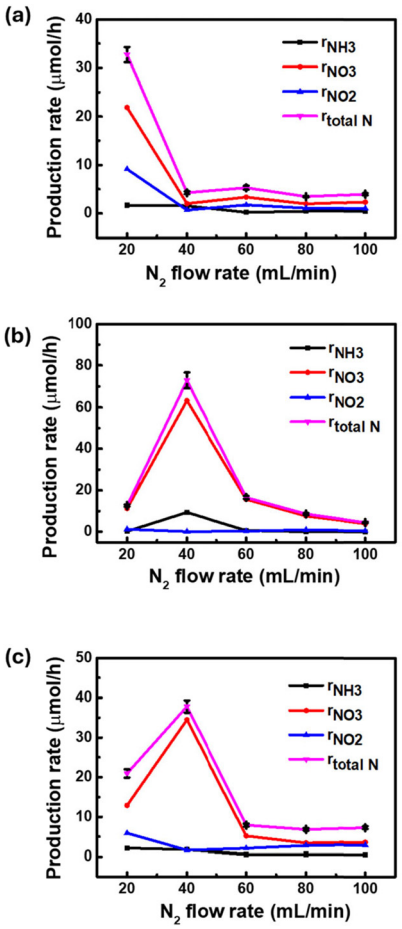

Fig. 9 Nitrogen fixation from N_2 and H_2O. (a) H_2O flowrate 0.05 mL min^{-1}; (b) H_2O flowrate 0.10 mL min^{-1}; (c) H_2O flowrate 0.15 mL min^{-1}, error bars indicate standard deviation.

oxygen species.[59] Compared with the catalytic performance with catalysts, the NH_3 production rates are improved from 9.40 to 10.08, 14.26, 12.18, and 11.67 μmol h^{-1} with the introduction of SBA-15, Ni-SBA-15, Fe-SBA-15, and Cu-SBA-15, respectively. Meanwhile the corresponding NO_2^- production rates are enhanced from 0.30 to 0.92, 4.74, 3.22 and 2.81, respectively. But the NO_3^- production rates have increased notably, especially with the addition of Ni-SBA-15, growing from 63.32 to 121.80, resulting in the highest total N production rate of 140.78 μmol h^{-1}. The metal on the support serves as the catalytically active site, which can reduce the N_2 bond energy by interacting with nitrogen molecules under the plasma condition so that nitrogen molecules are more easily broken, thus promoting nitrogen fixation reaction.[60] During the plasma discharge, Ni is reported as more favorable to activate nitrogen into nitrogen species than Fe and Cu, mainly due to the enhanced plasma discharge resulting in strengthened gas-phase radical reactions of N, H, OH, NH, and NO on the surface of the catalysts.[61,62] Fig. 10(b) displays the influence of the catalyst on the yield of total N, and the trend is identical to that of the production rate. The energy yield is employed to evaluate the energy consumption

in the reaction, another parameter to determine practical application. From Fig. 10(c), the energy yield of the reaction without a catalyst is 309.74 mg_N kW^{-1} h^{-1} with a power of 3.3 W. With the introduction of a catalyst, the energy yield of Ni-SBA-15 can reach 597.32 mg_N kW^{-1} h^{-1}, almost double that without a catalyst. This implies that less energy is required in the reaction because the catalyst effectively reduces the energy barrier of the reaction and improves the efficiency of the reaction.[63]

Catalyst stability is critical in chemical processes and industrial applications, influencing performance, longevity, and economic viability. In our experiment, stability tests of nitrogen fixation with N_2 and H_2O on the Ni-SBA-15 catalyst were performed by a continuous experiment of 12 h with 6 h plasma on and off. Generally, plasma reactions can be easily adjusted according to power grid fluctuations or peaks in real industrial applications, which can help optimize energy efficiency. The stability test result is exhibited in Fig. 11, displaying excellent stability over the tested conditions. It can be found that the total nitrogen production rate displayed good stability with only a 13.74% reduction over 12 h, which can be due to the oxidation of the catalysts.

Table 2 compares the energy cost of nitrogen fixation from N_2/air/O_2 and H_2O with different plasma types. Generally, the energy cost required in the nitrogen fixation liquid phase is dramatically higher than in the gas phase, which can be due to significant losses at the plasma–liquid interface. From the data in the table, the energy cost in our work is lower than others, indicating that our system is more economical, sustainable, and environmentally friendly. It can be found that the energy cost in our work is 162.72 MJ mol^{-1} without catalysts. When plasma–catalyst integration is applied, the energy cost declines remarkably to 84.35 MJ mol^{-1}, which might be attributed to the enhanced interaction between the reactive species. The energy cost remains higher than that of the Haber–Bosch process (approximately 0.5–0.6 MJ mol^{-1}) and the Birkeland–Eyde process (around 2.4–3.1 MJ mol^{-1}).[64] However, the DBD unit offers significant advantages, such as a compact electrical setup, easy switch control, and access to abundant raw materials, making it a promising solution for sustainable fertilizer production when powered by renewable energy sources like solar and wind.

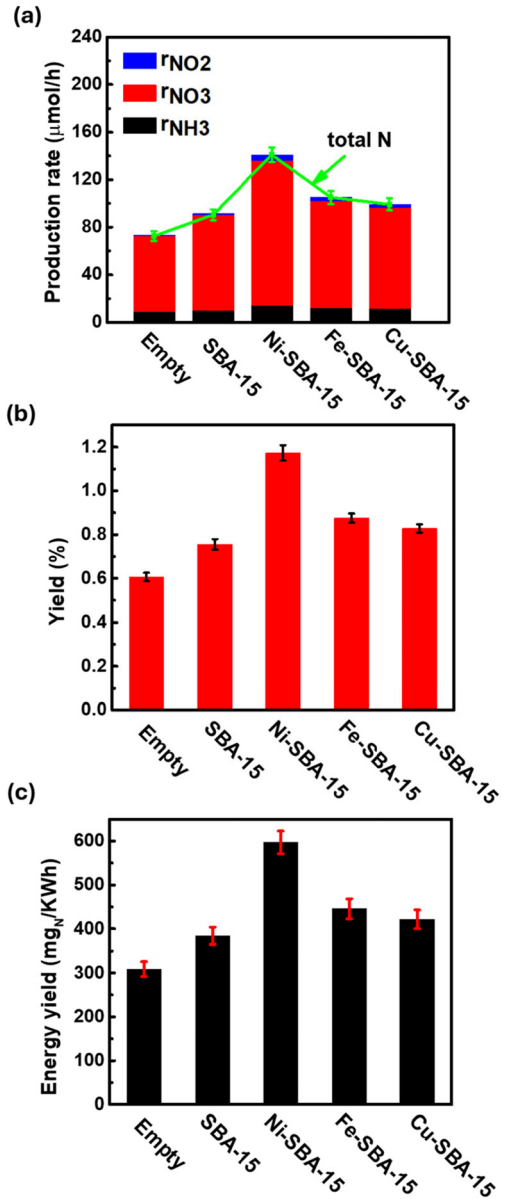

Fig. 10 (a) Production rate of NH_3, NO_3^-, and NO_2^- produced from N_2 and H_2O with and without catalysts, (b) yield and (c) energy yield of total N obtained from N_2 and H_2O with and without catalysts, error bars indicate standard deviation [reaction conditions: power of 3.30 W; N_2 flow rate of 40 mL min^{-1}, and H_2O flow rate of 0.1 mL min^{-1}].

Mechanism of nitrogen fixation by combined DBD plasma and catalyst

Understanding the reaction mechanism, especially the NTP plasma-assisted reaction between N_2 and H_2O, is vital for developing nitrogen fixation. Notwithstanding that much work has been done to understand the mechanism of the

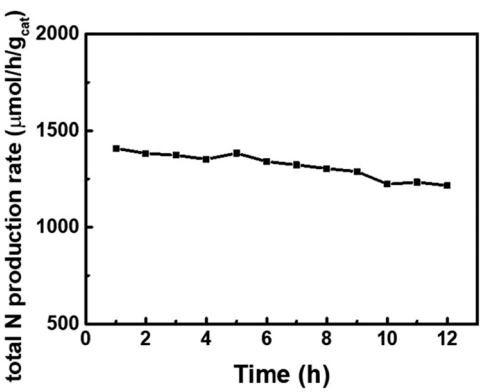

Fig. 11 Stability test of nonthermal plasma-assisted nitrogen fixation from N_2 and H_2O over the Ni-SBA-15 catalyst [reaction conditions: power of 3.30 W; N_2 flow rate of 40 mL min^{-1}, and H_2O flow rate of 0.1 mL min^{-1}].

Table 2 Comparative summary of our work with other studies on nitrogen fixation from N_2/air/O_2 contact with H_2O

Year	Plasma reactor	Gas	Energy cost (MJ mol^{-1})	Ref.
2021	AC DBD plasma	$N_2/O_2/H_2O$ mix	294	65
2020	Needle-water microplasma	$N_2/O_2/H_2O$	167.4	66
2022	Rotating electrodes plasma	N_2/H_2O	61.5	67
2020	Spark plasma	N_2/H_2O	95	68
2012	Pulsed rotating spark plasma	$N_2/O_2/H_2O$	186	30
2016	AC-gliding arc plasma	Air/water	3600	69
2025	Pulsed DBD plasma	N_2/H_2O	162.72	This work
	Pulsed DBD plasma packed with catalysts	N_2/H_2O	84.35	This work

plasma-assisted reaction between N_2, H_2, and O_2,[60,70,71] much work remains to be done. Simultaneously, replacing hydrogen with inexpensive and accessible water for nitrogen fixation is believed to change these reaction pathways.[72] The above experimental results demonstrate that the primary product is NO_x instead of NH_3, which is different from other research studies. Therefore, exploring a reasonable perception of the mechanism in the plasma-activated reaction between N_2 and H_2O is worthwhile. N_2 molecules can be activated by electron collision excitation (electronic excitation and vibration excitation), dissociation, and ionization in the plasma process, forming N_2^+, N_2^*, and N atoms (reactions (8)–(10)). Some researchers stated that heterogeneous catalysts can facilitate the dissociation of N_2 molecules,[73] which contributes to higher nitrogen oxidation or hydrogenation. Our experimental results for higher production rates in NH_3, NO_3^- and NO_2^- when plasma is integrated with catalysts prove this. H_2O molecules can be decomposed into OH, H, and O species in the plasma discharge zone, which is also confirmed by the work of our group and others (reactions (11) and (12)).[36,74,75] The production of NH_3 is obtained by the stepwise hydrogenation of N, presented in reactions (13)–(15), based on the Eley–Rideal (E–R) or Langmuir–Hinshelwood (L–H) mechanism. At the same time, the produced N species colloid with OH* or O* species, which can further form NO_x, HNO_3, and HNO_2 (reactions (16)–(21)). In addition, H_2O_2 might be generated by two OH and serve as an oxidant that reacts with NO_x to generate HNO_3 (reactions (22) and (23)).[29,76,77] According to our experimental results, the proportion of NO_3^- is higher than that of NH_3 and NO_2^-, which can be assigned to the reaction of HNO_2 with NH_3 to form NH_4NO_2, rapidly decomposing into N_2 and H_2O (reactions (24) and (25)).[29] Experimental results in OES prove that most NO species and N species were generated in Ni-SBA-15, demonstrating that more NH_3 and NO_x were created. The interaction between the nickel (Ni) metal and SBA-15 might affect the catalytic activity or electron density on the catalyst surface to dissociate N_2 and H_2O and lead to better nitrogen fixation efficiency.

$$e + N_2 \rightarrow N_2^* + e \quad (8)$$

$$e + N_2 \rightarrow N_2^+ + e \quad (9)$$

$$N_2 \rightarrow 2N \quad (10)$$

$$H_2O \rightarrow H^* + OH^* \quad (11)$$

$$OH^* \rightarrow O^* + H^* \quad (12)$$

$$N^* + H^* \rightarrow NH^* \quad (13)$$

$$NH^* + H^* \rightarrow NH_2^* \quad (14)$$

$$NH_2^* + H^* \rightarrow NH_3 \quad (15)$$

$$N^* + OH^* \rightarrow NO + H^* \quad (16)$$

$$NO + OH^* \rightarrow HNO_2 \quad (17)$$

$$NO_2 + OH^* \rightarrow HNO_3 \quad (18)$$

$$NO + O^* \rightarrow NO_2 \quad (19)$$

$$2O^* \rightarrow NO_2 \quad (20)$$

$$NO + NO + O_2 \rightarrow NO_2 \quad (21)$$

$$2OH^* \rightarrow H_2O_2 \quad (22)$$

$$2NO + H_2O_2 \rightarrow HNO_3 + H_2O \quad (23)$$

$$HNO_2 + NH_3 \rightarrow NH_4NO_2 \quad (24)$$

$$NH_4NO_2 \rightarrow N_2 + O_2 \quad (25)$$

Conclusions

In this work, ammonia (NH_3), nitrite (NO_2^-), and nitrate (NO_3^-) were successfully produced from a plasma-catalyst integrated system of nitrogen fixation with N_2 and H_2O. The catalysts of different metals, such as Ni, Fe, and Cu, were impregnated on the support of SBA-15 and applied in the reaction. The total nitrogen (summary of NH_3, NO_2^-, and NO_3^-) production rate can reach 140.78 μmol h^{-1} with an N_2 flow rate of 40 mL min^{-1}, a H_2O flow rate of 0.1 mL min^{-1}, and a low 3.3 W plasma integrated with Ni-SBA-15. The synergistic effect of plasma and catalyst promotes the production of total N and the energy yield. This work provides a good starting point for discussion and further

research of more effective catalyst design and mechanism investigation.

Data availability

The data supporting this article have been included as part of the ESI.†

Author contributions

Yanna Liu: conceptualization, investigation, writing – original draft; Zhaofei Li: resources, writing – review & editing; Hua Song: conceptualization, supervision, project administration, writing – review & editing.

Conflicts of interest

There are no conflicts to declare.

References

1 L. R. Winter and J. G. Chen, *Joule*, 2021, **5**, 300–315.
2 B. M. Hoffman, D. Lukoyanov, Z.-Y. Yang, D. R. Dean and L. C. Seefeldt, *Chem. Rev.*, 2014, **114**, 4041–4062.
3 G. E. D. Oldroyd and R. Dixon, *Curr. Opin. Biotechnol.*, 2014, **26**, 19–24.
4 J. K. Ladha, M. B. Peoples, P. M. Reddy, J. C. Biswas, A. Bennett, M. L. Jat and T. J. Krupnik, *Field Crops Res.*, 2022, **283**, 108541.
5 J. Bellenger, R. Darnajoux, X. Zhang and A. Kraepiel, *Biogeochemistry*, 2020, **149**, 53–73.
6 J. H. Montoya, C. Tsai, A. Vojvodic and J. K. Nørskov, *ChemSusChem*, 2015, **8**, 2180–2186.
7 N. Popov, *Plasma Sources Sci. Technol.*, 2016, **25**, 044003.
8 W. Wang, B. Patil, S. Heijkers, V. Hessel and A. Bogaerts, *ChemSusChem*, 2017, **10**, 2145–2157.
9 D. Kim, S. Surendran, Y. Lim, H. Choi, J. Lim, J. Y. Kim, M. K. Han and U. Sim, *Int. J. Energy Res.*, 2022, **46**, 4119–4129.
10 D. Kim, S. Surendran, G. Janani, Y. Lim, H. Choi, M.-K. Han, S. Yuvaraj, T.-H. Kim, J. K. Kim and U. Sim, *Mater. Lett.*, 2022, **314**, 131808.
11 T. Y. An, C. Xia, M. Je, H. Lee, S. Ji, M. C. Kim, S. Surendran, M. K. Han, J. Lim and D. K. Lee, *SusMat*, 2024, **4**, e226.
12 A. J. Medford and M. C. Hatzell, *ACS Catal.*, 2017, **7**, 2624–2643.
13 X. Xue, R. Chen, C. Yan, Y. Hu, W. Zhang, S. Yang, L. Ma, G. Zhu and Z. Jin, *Nanoscale*, 2019, **11**, 10439–10445.
14 D. Panchal, Q. Lu, K. Sakaushi and X. Zhang, *Chem. Eng. J.*, 2024, 154920.
15 K. Lu, Y. Xu, H. Yuan, J. Liang, H. Wang, J. Zhang, Y. Li and D. Yang, *Int. J. Hydrogen Energy*, 2025, **97**, 835–844.
16 S. Li, J. Medrano, V. Hessel and F. Gallucci, *Processes*, 2018, **6**, 248.
17 A. Bogaerts and E. C. Neyts, *ACS Energy Lett.*, 2018, **3**, 1013–1027.
18 J. Liu, L. Nie, D. Liu and X. Lu, *Plasma Processes Polym.*, 2024, **21**, 2300153.
19 Z. P. Qu, R. W. Zhou, J. Sun, Y. T. Gao, Z. Li, T. Q. Zhang, R. S. Zhou, D. X. Liu, X. Tu, P. Cullen and K. Ostrikov, *ChemSusChem*, 2024, **17**, e202300783.
20 B. Patil, N. Cherkasov, J. Lang, A. Ibhadon, V. Hessel and Q. Wang, *Appl. Catal., B*, 2016, **194**, 123–133.
21 Y. Wang, W. Yang, S. Xu, S. Zhao, G. Chen, A. Weidenkaff, C. Hardacre, X. Fan, J. Huang and X. Tu, *J. Am. Chem. Soc.*, 2022, **144**, 12020–12031.
22 F. Jardali, S. Van Alphen, J. Creel, H. A. Eshtehardi, M. Axelsson, R. Ingels, R. Snyders and A. Bogaerts, *Green Chem.*, 2021, **23**, 1748–1757.
23 X. Xu, M. Sun, Q. Song, G. Liu and H. Zhang, *J. Phys. D: Appl. Phys.*, 2024, **57**, 415206.
24 Z. Li, E. Wu, L. Nie, D. Liu and X. Lu, *Phys. Plasmas*, 2023, **30**, 083502.
25 O. S. Bahnamiri, C. Verheyen, R. Snyders, A. Bogaerts and N. Britun, *Plasma Sources Sci. Technol.*, 2021, **30**, 065007.
26 S. Kelly and A. Bogaerts, *Joule*, 2021, **5**, 3006–3030.
27 D. Zhou, R. Zhou, R. Zhou, B. Liu, T. Zhang, Y. Xian, P. J. Cullen, X. Lu and K. Ostrikov, *Chem. Eng. J.*, 2021, **421**, 129544.
28 S. Li, T. Van Raak and F. Gallucci, *J. Phys. D: Appl. Phys.*, 2019, **53**, 014008.
29 E. Vervloessem, M. Gromov, N. De Geyter, A. Bogaerts, Y. Gorbanev and A. Nikiforov, *ACS Sustainable Chem. Eng.*, 2023, **11**, 4289–4298.
30 W. Bian, X. Song, J. Shi and X. Yin, *J. Electrost.*, 2012, **70**, 317–326.
31 Y. Kubota, K. Koga, M. Ohno and T. Hara, *Plasma Fusion Res.*, 2010, **5**, 042.
32 T. Haruyama, T. Namise, N. Shimoshimizu, S. Uemura, Y. Takatsuji, M. Hino, R. Yamasaki, T. Kamachi and M. Kohno, *Green Chem.*, 2016, **18**, 4536–4541.
33 Z. Liu, Y. Tian, G. Niu, X. Wang and Y. Duan, *ChemSusChem*, 2021, **14**, 1507–1511.
34 I. Muzammil, Y.-N. Kim, H. Kang, D. K. Dinh, S. Choi, C. Jung, Y.-H. Song, E. Kim, J. M. Kim and D. H. Lee, *ACS Energy Lett.*, 2021, **6**, 3004–3010.
35 T. Zhang, R. Zhou, S. Zhang, R. Zhou, J. Ding, F. Li, J. Hong, L. Dou, T. Shao and A. B. Murphy, *Energy Environ. Mater.*, 2023, **6**, e12344.
36 W. Li, M. Cao, S. Meng, Z. Li, H. Xu, L. Liu and H. Song, *J. Cleaner Prod.*, 2023, **387**, 135913.
37 Q. Yao, Z.-H. Lu, K. Yang, X. Chen and M. Zhu, *Sci. Rep.*, 2015, **5**, 15186.
38 J. Shan, Y. Xue, D. Wang, Z. Chen and S. Zhu, *Appl. Catal., B*, 2022, **302**, 120870.
39 O. Daoura, G. Fornasieri, M. Boutros, N. El Hassan, P. Beaunier, C. Thomas, M. Selmane, A. Miche, C. Sassoye and O. Ersen, *Appl. Catal., B*, 2021, **280**, 119417.
40 C. F. Toncón-Leal, S. Amaya-Roncancio, A. A. Garcia Blanco, M. Moreno and K. Sapag, *Top. Catal.*, 2019, **62**, 1086–1095.
41 M. B. Gawande, A. Goswami, F.-X. Felpin, T. Asefa, X. Huang, R. Silva, X. Zou, R. Zboril and R. S. Varma, *Chem. Rev.*, 2016, **116**, 3722–3811.
42 Y. Li, K.-A. Min, B. Han and L. Y. S. Lee, *Appl. Catal., B*, 2021, **282**, 119548.

43 J. Hu, Z. Liu, Y. You, H. Zhang, X. Chen, Y. Sun, J. Zhang and G. Luo, *Colloid Interface Sci. Commun.*, 2023, **53**, 100703.
44 H. Liang, L. Zhang and H. Wu, *Small*, 2022, **18**, 2203620.
45 K. Chen, H. Fang, S. Wu, X. Liu, J. Zheng, S. Zhou, X. Duan, Y. Zhuang, S. C. E. Tsang and Y. Yuan, *Appl. Catal., B*, 2019, **251**, 119–129.
46 P. Chawdhury, K. Bhargavi, M. Selvaraj and C. Subrahmanyam, *Catal. Sci. Technol.*, 2020, **10**, 5566–5578.
47 M. F. Kamaruzaman, Y. H. Taufiq-Yap and D. Derawi, *Biomass Bioenergy*, 2020, **134**, 105476.
48 Z.-W. Wu, J. Xiong, C.-W. Wang and Y.-H. Qin, *Int. J. Hydrogen Energy*, 2023, **48**, 4728–4737.
49 B. Huang, Y. Chang, H. Wang and Z. Qu, *Chem. Eng. J.*, 2024, **484**, 149658.
50 K.-K. Miao, X.-L. Luo, W. Wang, J.-L. Guo, S.-F. Guo, F.-J. Cao, Y.-Q. Hu, P.-M. Chang and G.-D. Feng, *Microporous Mesoporous Mater.*, 2019, **289**, 109640.
51 A. Bhattacharyya and B. Rajanikanth, *IEEE Trans. Dielectr. Electr. Insul.*, 2015, **22**, 2907–2914.
52 C. Pan, S. Jun, R. Tangchun, Y. Tao and Y. Yongxiang, *Plasma Sci. Technol.*, 2017, **19**, 125505.
53 Q. Li, H. Takana, Y.-K. Pu and H. Nishiyama, *Appl. Phys. Lett.*, 2012, **100**, 133501.
54 G.-B. Zhao, M. D. Argyle and M. Radosz, *J. Appl. Phys.*, 2007, **101**, 033303.
55 K. Gazeli, P. Svarnas, B. Held, L. Marlin and F. Clement, *J. Appl. Phys.*, 2015, **117**, 093302.
56 R. W. B. Pearse, A. G. Gaydon, R. W. B. Pearse and A. G. Gaydon, *The identification of molecular spectra*, Chapman and Hall London, 1976.
57 P. Lamichhane, R. Paneru, L. N. Nguyen, J. S. Lim, P. Bhartiya, B. C. Adhikari, S. Mumtaz and E. H. Choi, *React. Chem. Eng.*, 2020, **5**, 2053–2057.
58 J. R. Toth, N. H. Abuyazid, D. J. Lacks, J. N. Renner and R. M. Sankaran, *ACS Sustainable Chem. Eng.*, 2020, **8**, 14845–14854.
59 S. Li, Y. Shao, H. Chen and X. Fan, *Ind. Eng. Chem. Res.*, 2022, **61**, 3292–3302.
60 B. S. Patil, N. Cherkasov, J. Lang, A. O. Ibhadon, V. Hessel and Q. Wang, *Appl. Catal., B*, 2016, **194**, 123–133.
61 Y. Wang, M. Craven, X. Yu, J. Ding, P. Bryant, J. Huang and X. Tu, *ACS Catal.*, 2019, **9**, 10780–10793.
62 P. Peng, C. Schiappacasse, N. Zhou, M. Addy, Y. Cheng, Y. Zhang, K. Ding, Y. Wang, P. Chen and R. Ruan, *ChemSusChem*, 2019, **12**, 3702–3712.
63 J. Sun, T. Zhang, J. Hong, R. Zhou, H. Masood, R. Zhou, A. B. Murphy, K. K. Ostrikov, P. J. Cullen, E. C. Lovell, R. Amal and A. R. Jalili, *Chem. Eng. J.*, 2023, **469**, 143841.
64 K. H. Rouwenhorst, F. Jardali, A. Bogaerts and L. Lefferts, *Energy Environ. Sci.*, 2021, **14**, 2520–2534.
65 N. C. Roy, C. Pattyn, A. Remy, N. Maira and F. Reniers, *Plasma Processes Polym.*, 2021, **18**, 2000087.
66 C. Pattyn, N. Maira, A. Remy, N. C. Roy, S. Iséni, D. Petitjean and F. Reniers, *Phys. Chem. Chem. Phys.*, 2020, **22**, 24801–24812.
67 X. Lei, H. Cheng, L. Nie and X. Lu, *Plasma Chem. Plasma Process.*, 2022, 1–17.
68 Y. Gorbanev, E. Vervloessem, A. Nikiforov and A. Bogaerts, *ACS Sustainable Chem. Eng.*, 2020, **8**, 2996–3004.
69 J. Yang, T. Li, C. Zhong, X. Guan and C. Hu, *J. Electrochem. Soc.*, 2016, **163**, E288.
70 E. Vervloessem, M. Aghaei, F. Jardali, N. Hafezkhiabani and A. Bogaerts, *ACS Sustainable Chem. Eng.*, 2020, **8**, 9711–9720.
71 C. Ndayirinde, Y. Gorbanev, R. G. Ciocarlan, R. De Meyer, A. Smets, E. Vlasov, S. Bals, P. Cool and A. Bogaerts, *Catal. Today*, 2023, **419**, 114156.
72 Z. Z. Huang, A. Xiao, D. W. Liu, X. P. Lu and K. Ostrikov, *Plasma Processes Polym.*, 2022, **19**, e2100198.
73 K. H. Rouwenhorst, H. G. Burbach, D. W. Vogel, J. N. Paulí, B. Geerdink and L. Lefferts, *Catal. Sci. Technol.*, 2021, **11**, 2834–2843.
74 M. Varne, G. R. Dey and T. N. Das, *Int. J. Hydrogen Energy*, 2016, **41**, 22769–22774.
75 M. Younas, S. Shafique, A. Faisal, A. Hafeez, F. Javed, M. Mustafa and F. Rehman, *Fuel*, 2023, **331**, 125838.
76 Y. Gorbanev, D. O'Connell and V. Chechik, *Chem. – Eur. J.*, 2016, **22**, 3496–3505.
77 J. Fujera, T. Homola, V. Jirásek, J. Ondrácek, B. Tarabová, V. Prukner and M. Simek, *Plasma Sources Sci. Technol.*, 2024, **33**, 075002.

